Buried palaeo-polygonal terrain detected underneath Utopia Planitia on Mars by the Zhurong radar

Lei Zhang [1,2,14], Chao Li [1,2,14], Jinhai Zhang [1,2] ✉, Bin Zhou [3,4], Yu-Yan Sara Zhao [5,6,7], Yang Liu [7,8], Kaichang Di[7,9], Ross N. Mitchell [10,11], Juan Li[2,11], Zhigang Zhang[2,11], Lin Chen [10], Xiaofeng Liang [10], Weijia Sun [2], Yike Liu[12], Xu Zhao[2], Jinlai Hao[2], Changyi Xu[2], Yikang Zheng [12], Yibo Wang[12], Xin Wang [2], Pan Zhao[10], Wenmin Lv[1], Yang Li [10], Haiqiang Lan[10], Yuxi Li[3], Wei Wang [2], Yang Lu[13], Honglei Lin [2], Peng Fang [1], Wei Lin [2], Yong Wei [2,11], Ling Chen [10,11], Guangyou Fang[3,4], Yangting Lin[2], Zhenxing Yao[2] & Yongxin Pan[2,11]

As the largest basin on Mars, Utopia Planitia has both experienced and recorded variations of the Martian palaeoclimate. Layered subsurface structures have been identified by ground-penetrating radar in southern Utopia Planitia but lateral variations of the subsurface, potentially linked to the Martian palaeoclimatic evolution, have not been investigated. Here we report the lateral frequency-variation patterns of Zhurong radar reflections and interpret them as buried polygonal terrain below a depth of 35 m. Sixteen polygonal wedges were identified within ~1.2 km distance, suggesting a wide distribution of such terrain under Utopia Planitia. The contrast above and below ~35 m depth represents a notable transformation of aqueous activity or thermal conditions in the Late Hesperian–Early Amazonian. The interpreted buried polygons, possibly generated by freeze–thaw cycles, imply that there was a strong palaeoclimatic variability at low-to-mid latitudes (~25° N), potentially due to the high obliquity of ancient Mars.

Utopia Planitia, the largest impact basin in the northern hemisphere of Mars[1], is considered to be a Late Hesperian lowland unit[2] (Fig. 1a). The northern lowlands were largely filled with materials of the Vastitas Borealis Formation (VBF)[3] as a sublimation residue from frozen ponded bodies of water[4] and subsequently modified by Amazonian resurfacing[5], such as long-term weathering, aeolian deposition[6,7] and impact remixing[8]. A large number of orbital and in situ geomorphometry measurements show that polygonal terrain[9,10] (Fig. 1c–f) and other periglacial features[11,12] are extensively distributed in southern and western Utopia Planitia, indicating the occurrence of water-related or ice-related activities[13,14]. Viking 2, a previous ground-based probe in northern Utopia Planitia

(Fig. 1a), identified troughs that probably form a polygonal network[15]. In 2021, two rovers, Perseverance and Zhurong (Fig. 1a and Extended Data Fig. 1), landed on Mars almost simultaneously[16,17]. Both rovers are equipped with ground-penetrating radar (GPR), operating at a frequency range of 150–1,200 MHz for Perseverance and 15–95 MHz (low-frequency channel) and 450–2,000 MHz (high-frequency channel) for Zhurong[18,19]. These can detect, for the first time, the high-resolution subsurface structures of Jezero crater[20] and southern Utopia Planitia[21,22], respectively. As an important complement to orbital radar explorations[23,24], in situ GPR surveying can provide critical local details of shallow structures and composition within approximately 100 m depth along a rover traverse.
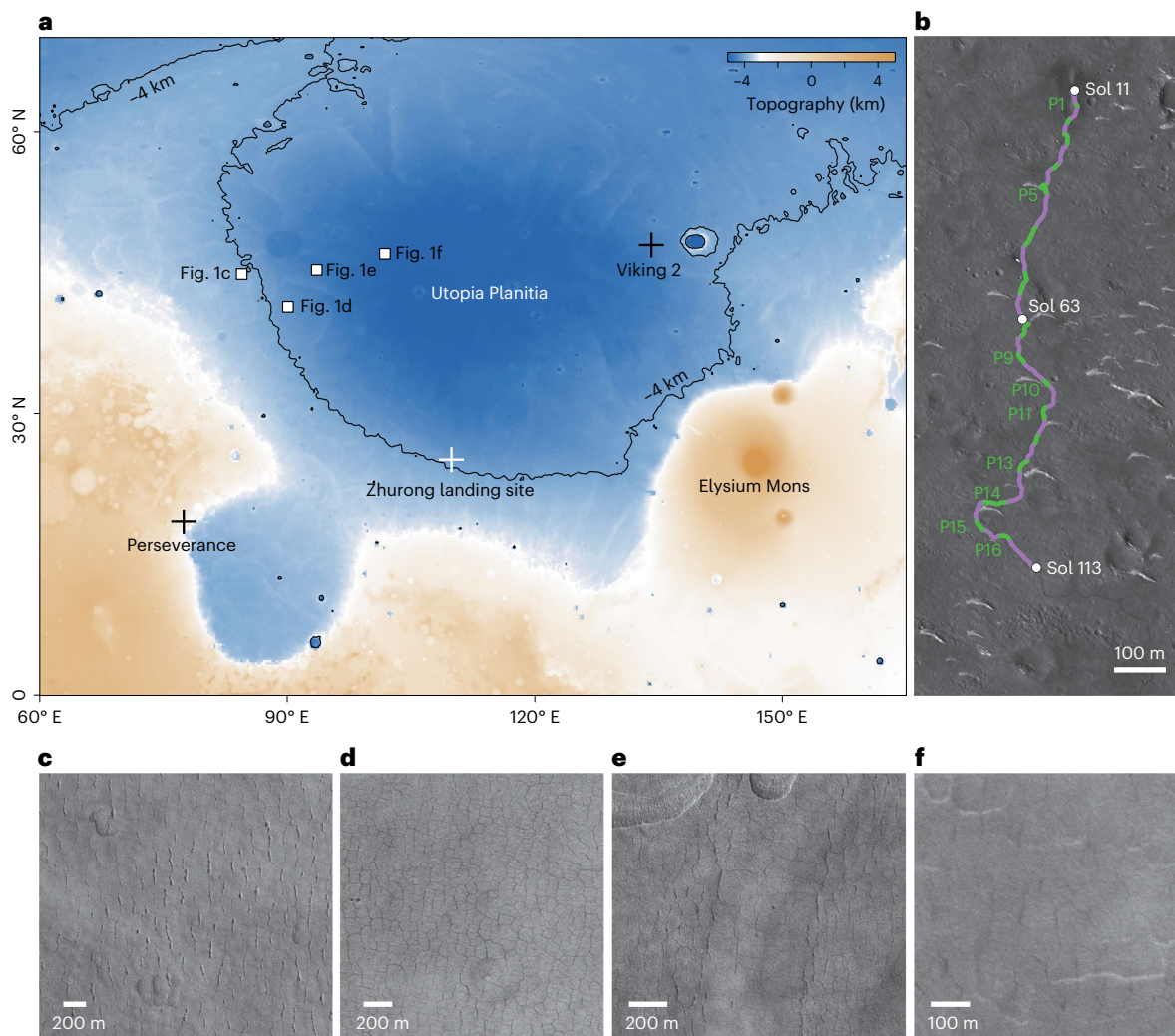
Fig. 1 | **Zhurong rover landing site and images of polygonal terrain in Utopia Planitia. a**, Topographic map of Utopia Planitia, showing the landing sites of the Zhurong rover, the Viking 2 lander and the Perseverance rover. The −4 km elevation contour is shown. Four local regions (**c**–**f**) with polygonal terrain are marked with white squares. **b**, The Zhurong rover traverse from Sol 11 through Sol 113 (HiRISE image: ESP_073225_2055). Green segments denote the wedges of buried polygons recognized from Fig. 2 (P1–P16). Purple segments denote the interiors of the polygons. **c**–**f**, Four representative HiRISE images of polygons in Utopia Planitia whose locations are marked in **a**: PSP_002202_2250 (**c**), PSP_006962_2215 (**d**), PSP_002162_2260 (**e**) and PSP_003177_2275 (**f**). Note the range of spatial scales for the sizes of the polygons. The average diameters of polygons shown in **c**–**f** are calculated in Extended Data Fig. 6. Credit for HiRISE images: NASA/JPL/University of Arizona.

The Zhurong landing site is thought to be one of the best places for detecting ground ice at low-to-mid latitudes on Mars[25]. The GPR onboard Zhurong rover, thus, provides an unprecedented opportunity to illuminate subsurface structures and to investigate geological processes, particularly those associated with ancient or current water-related activities in southern Utopia Planitia. Subsurface layering in Utopia basin of Mars has been revealed by the radar of the Zhurong rover[21,22], indicating the presence of sedimentation due to episodic hydraulic flooding that is interpreted to represent the basin infilling of Utopia Planitia during the Late Hesperian to Amazonian. However, previous works mainly focused on the vertically layered subsurface structure and less attention has been paid to lateral variations along the Zhurong radar profile.

Subsurface features potentially revealed in lateral variations are equally critical compared with the vertical layered structures for discovering the geological evolution of Mars. However, in the presence of strong scattering effects, preliminary attempts to extract features from the lateral variation of the Zhurong GPR profile proved unsuccessful. In an effort to unveil potential characteristics of the lateral variation of the subsurface surrounding the landing site, we conducted a comprehensive time–frequency analysis (Methods) of the Zhurong GPR data (Extended Data Figs. 2 and 3). We identified 16 nearly vertical bands dominated by anomalous low-frequency components at depths of 35–65 m along the rover traverse (Fig. 1b), which probably formed on ancient Mars and were buried by later geological processes.

Palaeo-polygons detected by the GPR on the Zhurong rover

Figure 2a shows the frequency distribution in the depth domain after random noise attenuation[26] and time-to-depth conversion using the velocity model of ref. 21 (Methods). According to the features in the frequency variation with increasing depth, the subsurface structure can be divided into three layers: (1) the first layer (0–35 m) has uniformly distributed energy, indicating relatively homogeneous media; (2) the second layer (35–65 m) has a series of vertical bands with anomalous low-frequency components, indicating strong lateral variations; and (3) the third layer (65–80 m) is dominated by strong random noise, where the frequency increases anomalously and precludes further
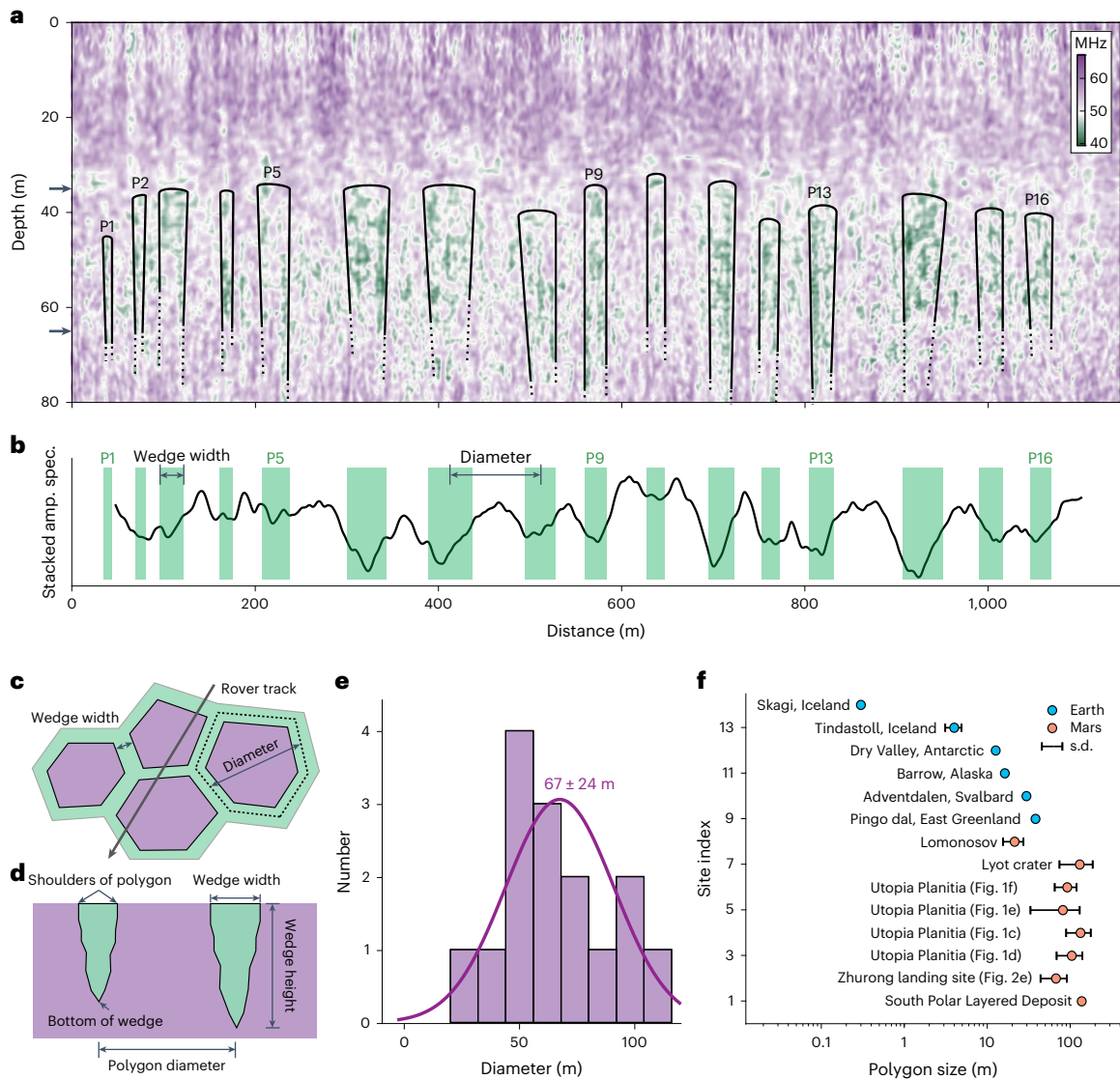
Fig. 2 | Time-varying average frequency distribution of the GPR data revealing buried polygons. a, Time-varying average frequency of the denoised GPR profile using the f–x regularized nonstationary autoregression method[26]. Green segments (P1–P16) denote the wedges of buried polygons. **b**, Stacked amplitude spectrum (amp. spec.; black curve) produced by summing the time-varying average frequency along each trace for depths of 35–65 m, which is roughly the depth range between the tops and bottoms of the observed polygons (black arrows in **a**). Green rectangles marked at both local minima of the stacked amplitude spectrum and the lower frequencies in **a** indicate the polygon wedges.

c, Sketch map as an example of what the buried polygonal terrain could look like from an aerial view. The rover traverse might be parallel to, perpendicular to or intersecting with the wedges of different polygons (Fig. 1b). **d**, Sketch map showing the definitions of polygon features. **e**, Histogram of polygon diameter recognized from **b**. **f**, Comparison of polygon size between Earth and Mars (literature references provided in Extended Data Fig. 7). Some data are presented as mean values ± standard deviation (s.d.). The Zhurong landing site data are from the measurements made in this study.

interpretation. The most notable feature in the GPR profile is the alternating occurrence of high- and low-frequency bands within the depth range 35–65 m in the second layer (Fig. 2a). The dominant frequency of these low-frequency bands (~45 MHz) is ~7 MHz lower than that of the background (~52 MHz) (Extended Data Fig. 3). Along the 1.2-km-long rover traverse, as many as 16 such low-frequency bands were identified (Figs. 1b and 2b).

We conducted a series of analyses to make sure that these low-frequency bands were not artefacts (Methods). First, the time-varying average frequency of the original GPR data without random noise attenuation (Extended Data Fig. 2c) shows similar low-frequency bands. Second, different denoising methods (Extended Data Fig. 2d, ref. 27) and segmentation methods (Extended Data Fig. 4) show consistent low-frequency bands (Fig. 2a), suggesting that none of

these low-frequency bands is an artefact from improper data processing. Additionally, the low-frequency bands generally start from a depth of ~35 m, not from the surface, indicating that they are associated with underground structures rather than surface objects. Furthermore, the positions of these low-frequency bands along the rover traverse (green segments in Fig. 1b) do not show any correlation with the distribution of dunes or rocks on the surface (Extended Data Fig. 1), suggesting that the low-frequency bands are not caused by surface-related features. Therefore, we can confirm that the low-frequency bands faithfully reflect the lateral variations of subsurface structures. Considering that these anomalous structures systematically occur every few tens of metres and are nearly vertical in orientation (Fig. 2), we interpret them as the infilled wedges between columns of a polygonal terrain buried under ~35 m of overlying materials (Fig. 3).
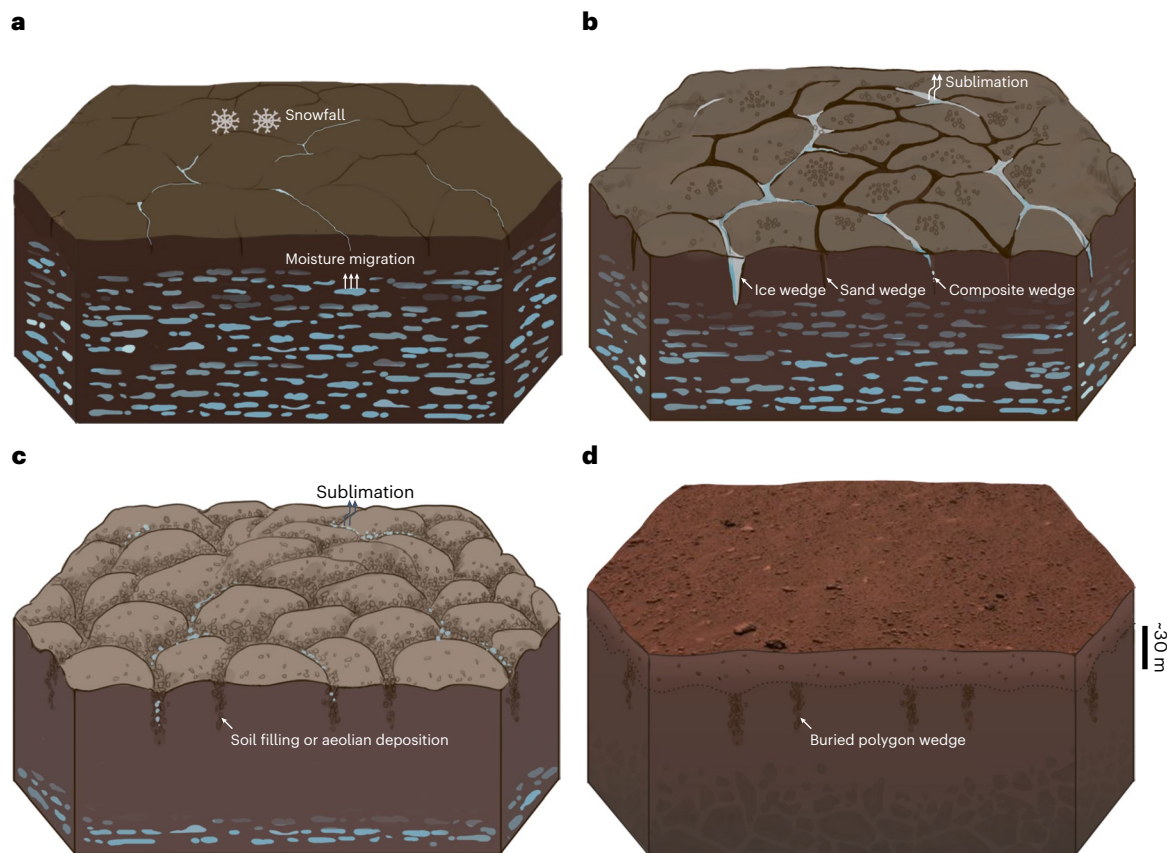
Fig. 3 | Schematic model of the polygonal terrain formation process at the Zhurong landing site. a, The origination of thermal contraction cracking on the surface. **b**, The formation of cracks infilled by water ice or soil material, causing three types of polygonal terrain (ice-wedge, composite-wedge and sand-wedge polygons). **c**, The stabilization of the surface polygonal terrain in the Late Hesperian–Early Amazonian, possibly with the cessation of an ancient wet environment. **d**, The palaeo-polygonal terrain, either with or without being eroded, was subsequently buried by deposition of the covering materials in the Amazonian. The Mars surface image was acquired by the Navigation and Terrain Camera (NaTeCam).

Tens of giant troughs have been identified near the Zhurong landing site[28]. These troughs are part of the polygonal trough system in southern Utopia Planitia[29]. Compared to polygonal terrain that is in the form of a network, isolated troughs usually exhibit linear shapes. Several isolated troughs have been observed with widths >100 m around the Zhurong landing site (Extended Data Fig. 5). However, no polygonal terrain has been identified from surface observations or orbital imagery (Fig. 1b) within several kilometres of the Zhurong landing site (Extended Data Fig. 1). Thus, the buried polygons observed here from the GPR profile exclusively represent a palaeo-polygonal terrain. The average polygon diameter extracted from the GPR profile (Fig. 2c,d) is ~67 m (Fig. 2e), which is within the typical range of previously reported Martian polygons (Fig. 2f) and is comparable to that of the surface polygons observed in western Utopia Planitia (Fig. 1c–f) within the latitudinal range between 40° and 50° (Methods and Extended Data Figs. 6 and 7). Considering that the direction of the rover track could be randomly oriented either perpendicular, parallel or oblique to the orientation of the polygon wedges (Extended Data Fig. 8), the average apparent width of the polygon wedges (~27 m) is regarded as an overestimate so that the actual average width should be narrower. The average height of the polygon wedges (the absolute elevation difference between the bottom of a wedge and the shoulder of a polygon) is ~30 m, corresponding to a polygon diameter/wedge height ratio of ~2.2, which is generally consistent with the theoretical polygon diameter/wedge height ratio (~3.0) of polygonal terrain[30]. The materials within the polygon wedges, possibly unconsolidated soil-rock mixtures, are more likely to absorb or scatter high-frequency components of radar waves, thus producing local low-frequency anomalies. In contrast, the polygon interiors are probably composed of well-consolidated materials, thus the high-frequency components can be well retained (Fig. 2a), leading to a weaker attenuation of radar waves.

Possible origin of the buried polygons

Polygonal terrain has been reported mainly in cold regions on Earth and mid-to-high latitudes on Mars[9,11,31,32]. Previously, Martian polygonal terrain has been observed only on the surface, mainly distributed at latitudes >30° (Fig. 1c–f; ref. 33), with diameters ranging from centimetres to kilometres[9,34]. Large Martian polygons (usually kilometre-scale) are widespread in the northern lowlands of Mars[35,36]. They were potentially caused by contraction jointing from lava cooling, contraction cracking from clay desiccation, thermal contraction, tectonic fracturing or the coalescence of smaller polygons[9,37,38]. In contrast, small-scale polygonal terrain (centimetres to tens of metres) was first found in situ by Viking 2, where the polygonal diameter near the lander was <10 m (ref. 31).

For polygons with diameters from centimetres to tens of metres, possible formation mechanisms[31,39,40] may include contraction from desiccation of wet sediments producing mud-cracks, contraction from cooling lava producing columnar jointing, faulting creating a jointing system in rock and thermal contraction cracking. Polygonal cracks of desiccation-induced contraction are dominated by the evaporation of water in the soil, usually with a ratio of the crack width to the polygon diameter of <0.1 (refs. 41,42), which is much smaller than 0.4, the ratio of the wedge width (~27 m) to the polygon diameter (~67 m) detected in this paper. Consequently, desiccation as a contraction mechanism

can be ruled out. In addition, if the buried polygons were caused by the contraction of cooling lava, the reflections from the interfaces between the lava flow(s) and underlying and overlying sediments should be notable due to a strong dielectric contrast[43]. However, no such strong reflection interfaces were observed in the low-frequency GPR data (Extended Data Fig. 2a) or in the SHARAD data (Extended Data Fig. 9). In addition, there is no evidence for the presence of basaltic extrusions in the Zhurong landing area, suggesting that volcanic columnar jointing is an unlikely explanation. Faulting-generated jointing systems are typically long and linear in shape[40]. Moreover, the low-frequency bands appear intermittently over relatively short segments of the rover path (such as P10 to P11, P13 to P14, and P14 to P15 in Fig. 1b), instead suggesting a polygonal terrain. Additionally, the lengths and widths of jointing systems due to faulting are usually kilometres in scale, but the SHARAD profile across the Zhurong landing site (Extended Data Fig. 9) does not show any evident reflection in this region. Consequently, fault jointing as a cracking mechanism can also be ruled out. Therefore, by a process of elimination, the buried polygons are interpreted to have most likely formed by thermal contraction cracking. The cracks generated in the ground may be infilled by water or soil material, causing three types of polygonal terrain (ice-wedge, composite-wedge and sand-wedge polygons[44], Fig. 3b). Ice-wedge polygons usually develop in permafrost, with ice infilling the wedges[45]. The ice in a wedge could sublimate and local gravel, sand and clay particles could then partially fill in the wedge[46,47], so that composite-wedge polygons form. Sand wedges usually form in cold regions from initial thermal contraction with subsequent aeolian deposition in the wedges[48]. We next consider the implication of the proposed explanation.

Geological age constraints indicate that the previously reported polygons at the surface of Utopia Planitia mainly formed in the Hesperian[3,31]. Near the latitude of the Zhurong landing site, polygons possibly formed in the Hesperian and were then covered by materials from the Late Hesperian to Amazonian plains[1,2]. At the Zhurong landing site, the material at depths of 30–80 m could have formed in the Late Hesperian–Early Amazonian, consistent with crater-counting ages estimated over various spatial ranges in southern Utopia Planitia[5,28,29,49]. In addition, the dielectric permittivity in this depth range is like that of materials of the VBF, indicating that this layer may represent an upper portion of the VBF deposits[21]. As the wedges of the polygons occur at depths of 35–65 m (Fig. 2a), the buried polygonal terrain probably developed from the sedimentary materials of the VBF, under dramatic changes in surface temperature on early Mars[50]. Polygonal terrain is distributed on the surface of present-day Mars mainly in high-latitude regions (generally >30°; ref. 31), whereas the buried polygonal terrain detected by the Zhurong rover occurs at low-to-mid latitudes (25° N; Fig. 3d). This latitudinal contrast may indicate that the Zhurong landing site had a cold environment that is found only at high latitudes on present Mars, but in the Late Hesperian–Early Amazonian, allowing for the formation of the palaeo-polygonal terrain at low-to-mid latitudes.

Implications for the palaeoclimatic conditions on Mars

The above-mentioned formation mechanism for the buried palaeo-polygonal terrain requires a cold environment and might be related to water/ice freeze–thaw processes in southern Utopia Planitia on early Mars. The detected buried polygons, which indicate that freezing occurred at low-to-mid latitudes, require strong palaeoclimatic variability, potentially due to the higher obliquity than today[51]. The possible presence of water and ice required for the freeze–thaw process in the wedges (Fig. 3a) may have come from cryogenic suction-induced moisture migration from an underground aquifer on Mars[52–54], snowfall from the air[55] or vapour diffusion for pore ice deposition.

The contrast in the lateral frequency-variation patterns above and below ~35 m depth (Fig. 2a) suggests that for the polygons to form and become buried, there was a critical transformation of aqueous

activity or thermal conditions in the Late Hesperian–Early Amazonian. This stark environmental transition at ~35 m, thus, may indicate both the cessation of an ancient wet environment (Fig. 3c) as well as that unknown notable geological events occurred after the formation of the polygonal terrain[56]. The depositional thickness and the age of the present surface materials at the Zhurong landing site could be roughly estimated by a geological survey of this region[5]. However, the role of erosion in the area is difficult to constrain. The continued acquisition of in situ data by the Zhurong rover will help better constrain the local dynamics of deposition and erosion. The tops of the polygons are at different depths (Fig. 2a), and smooth lateral changes in depth from the top of one polygon to the next exhibit broad peaks and valleys that may imply erosion before they were buried. Whether the buried polygonal terrain experienced subsequent erosion or not, the ~35-m-thick overlying materials provide a new constraint for estimating the deposition rate in southern Utopia Planitia.

Lateral variations in the subsurface structure at the Zhurong landing site provide evidence of a buried palaeo-polygonal terrain that formed in the Late Hesperian–Early Amazonian from periglacial processes. Occurring at low latitudes (~25° N), the polygonal terrain, which is interpreted as having most likely formed by thermal contraction cracking, makes a compelling case for the high obliquity of early Mars. The subsurface structure with the covering materials overlying the buried palaeo-polygonal terrain suggests that there was a notable palaeoclimatic transformation some time thereafter.

Methods

Time–frequency analysis and time-varying average frequency

GPR is an ideal instrument for exploring subsurface structures on Earth and extraterrestrial bodies. Electromagnetic waves are emitted on the surface and reflections are received from subsurface interfaces where the dielectric permittivity or conductivity changes. Although rover-based GPR has a limited detection range and penetrating depth, it is an effective tool for detecting shallow subsurface structures and has been successfully applied to both the near and far sides of the Moon[57,58]. The GPR data employed in this study are the low-frequency channel data with a frequency range of 15–95 MHz, which can penetrate a depth of 80 m below the Martian surface. The local time–frequency decomposition method is an effective form of time–frequency analysis. It has a higher temporal resolution than the widely used short-time Fourier transform method and S-transform method[59]. The main idea of local time–frequency decomposition is to use a Fourier basis to match nonstationary signals by solving a regularized least-squares minimization problem. A casual nonstationary signal $f(t)$, $t \in [0, L]$, can be expressed as a Fourier series as follows:

$$f(\mathrm{t}) = \sum_{n=-\infty}^{\infty} A_n(t)\psi_n(\mathrm{t}), \tag{1}$$

where $A_n(t)$ are the Fourier coefficients and $\psi_n(\mathrm{t}) = e^{i(2\pi nt/L)}$. We can obtain $A_n(t)$ by solving the least-squares minimization problem:

$$\min_{A_n} \left\| f(t) - \sum_n A_n(t)\psi_n(\mathrm{t}) \right\|_2^2. \tag{2}$$

However, the minimization problem is ill-posed because it is severely underconstrained. To solve this problem, a regularization term is needed. After adding a regularization operator R, the formal solution $\bar{A}_n(t)$ is given by:

$$\bar{A}_n(t) = \min_{A_n} \left\| f(t) - \sum_n A_n(t)\psi_n(\mathrm{t}) \right\|_2^2 + \mathrm{R}. \tag{3}$$

The absolute value of $\bar{A}_n(t)$ is the time–frequency representation of the signal $f(t)$, which we refer to as the time–frequency map.

Additionally, the time–frequency map can be converted to a time-varying average frequency according to

$$f_a(t) = \frac{\int f F^2(f,t)\,\mathrm{d}f}{\int F^2(f,t)\,\mathrm{d}f}, \qquad (4)$$

where $f_a(t)$ is the time-varying average frequency, $F(f,t)$ is the time–frequency map, and f and t are the frequency and time, respectively. The time-varying average frequency can show well the spatial-temporal distribution characteristics of the main frequency components and, thus, is widely used to extract subsurface attributes[60–62].

Potential causes of the anomalous low-frequency bands

To ensure that the identification of the anomalous low-frequency bands (Fig. 2a) was robust, we consider all their potential causes in this section. There are three possibilities for a horizontal discontinuity of the time-varying average frequency: (1) numerical artefacts caused by improper data processing, (2) an energy change in the GPR profile caused by surface anomalies, such as undulating terrain or surface rocks and (3) subsurface high-frequency-absorbing materials with an uneven transverse distribution. To avoid potential numerical artefacts and maintain the original proportion of the GPR profile energy in the horizontal direction during data processing, we used the same data processing methods, such as decoding, denoising and amplitude compensation, for all GPR data. The f–x regularized nonstationary autoregression method[26] and the streaming orthogonal prediction filter method[27] are both commonly used denoising methods in exploration seismic data processing, as they are effective in suppressing random noise and preserving weak signals. Therefore, item (1) should not be the case.

Furthermore, the travel path of the Zhurong rover was generally flat in terms of topography[63]. Within the first kilometre of the rover traverse, the fluctuation (within the local 3 m area covered by the rover) was no more than 0.1 m (Extended Data Fig. 1; ref. [64]). Moreover, the engineering team guiding the rover tried to avoid rocks, grooves, pits and other terrain during path planning, so the impact of surface rocks and undulating terrain was mostly eliminated. The images taken by the Navigation and Terrain Camera (NaTeCam)[65] show no evident variation in the terrain along the rover path except for several relatively bright white dune structures. This analysis shows that the horizontal discontinuity of the GPR profile was negligibly affected by data processing and surface factors, so that it faithfully reflects the high-frequency attenuation or absorbing effects of subsurface materials.

Determination of the polygon diameters

To determine the polygon diameters in the GPR profile (Fig. 2a), the recognition process was based on the width of the anomalous low-frequency bands as follows. Step 1: According to Fig. 2a, the depth range of these anomalous low-frequency bands is roughly 35–65 m. Thus, the frequency values within this depth range were stacked and smoothed to obtain a stacked amplitude spectrum by summing the time-varying average frequency (Fig. 2a). Step 2: Local minima in the stacked amplitude spectrum curve were identified. The left and right boundaries of the low-frequency bands were determined using the frequency distribution diagram in Fig. 2a. Step 3: The polygon diameter and the width of the wedge between two adjacent polygons were calculated using the left and right boundaries of the low-frequency bands. The diameter of a polygon was defined as the distance between the middle positions of two adjacent low-frequency bands (Fig. 2b), and the width of the wedge between the polygons is the width of a low-frequency band.

For the High Resolution Imaging Science Experiment (HiRISE) images (Extended Data Fig. 6), the polygons were recognized using the following five steps. Step 1: Calibrate the scale of the HiRISE images. Step 2: Identify the boundaries of polygons in the HiRISE images.

Step 3: Mark the polygons using the imaging processing technology of the crack network to quantify crack patterns[66,67]. Step 4: Calculate the average diameter (unit: pixel) by averaging the maximum and minimum Feret diameters[68] of each polygon cell. Step 5: Calculate the normal distribution statistics for the diameters of all polygons to obtain their mean value and standard deviation (Extended Data Fig. 6).

Data availability

The Mars Rover Penetrating Radar data used in this study are available from the Lunar and Planetary Data Release System (https://clpds.bao.ac.cn/web/enmanager/home). Path to access the data: Home Page>Scientific Data>Mars. HiRISE images used in this paper are publicly available on NASA's Planetary Data System website (https://pds.nasa.gov). The SHARAD data used in this study are part of the Reduced Data Records produced by the US SHARAD Science Team and are available from the Planetary Data System (http://pds-geosciences.wustl.edu/missions/mro/SHARAD.htm). Other datasets generated and analysed in this study are available from the corresponding author upon reasonable request. Source data are provided with this paper.

Code availability

The codes used in this study are available to interested researchers upon request.

References

1. McGill, G. E. Buried topography of Utopia, Mars: persistence of a giant impact depression. *J. Geophys. Res. Solid Earth* **94**, 2753–2759 (1989).
2. Tanaka, K. L., Robbins, S. J., Fortezzo, C. M., Skinner, J. A. & Hare, T. M. The digital global geologic map of Mars: chronostratigraphic ages, topographic and crater morphologic characteristics, and updated resurfacing history. *Planet. Space Sci.* **95**, 11–24 (2014).
3. Tanaka K. L., Skinner J. A. & Hare T. M. *Geologic Map of the Northern Plains of Mars*, Vol. 2888 (US Department of the Interior, US Geological Survey, 2005); https://pubs.usgs.gov/sim/2005/2888/
4. Kreslavsky, M. A. & Head, J. W. Fate of outflow channel effluents in the northern lowlands of Mars: the Vastitas Borealis Formation as a sublimation residue from frozen ponded bodies of water. *J. Geophys. Res. Planets* **107**, 4-1–4-25 (2002).
5. Wu, X. et al. Geological characteristics of China's Tianwen-1 landing site at Utopia Planitia, Mars. *Icarus* **370**, 114657 (2021).
6. Gou, S. et al. Transverse aeolian ridges in the landing area of the Tianwen-1 Zhurong rover on Utopia Planitia, Mars. *Earth Planet. Sci. Lett.* **595**, 117764 (2022).
7. Liu, J. et al. Martian dunes indicative of wind regime shift in line with end of ice age. *Nature* **620**, 303–309 (2023).
8. Fairén, A. G. et al. Evidence for Amazonian acidic liquid water on Mars—a reinterpretation of MER mission results. *Icarus* **57**, 276–287 (2009).
9. Hiesinger, H. & Head, J. W. Characteristics and origin of polygonal terrain in southern Utopia Planitia, Mars: results from Mars Orbiter Laser Altimeter and Mars Orbiter Camera data. *J. Geophys. Res. Planets* **105**, 11999–12022 (2000).
10. Buczkowski, D. L., Seelos, K. D. & Cooke, M. L. Giant polygons and circular graben in western Utopia basin, Mars: exploring possible formation mechanisms. *J. Geophys. Res. Planets* **117**, E08010 (2012).
11. Morgenstern, A. et al. Deposition and degradation of a volatile-rich layer in Utopia Planitia and implications for climate history on Mars. *J. Geophys. Res. Planets* **112**, E06010 (2007).
12. Lefort, A. et al. Observations of periglacial landforms in Utopia Planitia with the high resolution imaging science experiment (HiRISE). *J. Geophys. Res. Planets* **114**, E04005 (2009).

13. Xiao, L. et al. Evidence for marine sedimentary rocks in Utopia Planitia: Zhurong rover observations. *Natl Sci. Rev.* **10**, nwad137 (2023).

14. Zhao, Y.-Y. S. et al. In situ analysis of surface composition and meteorology at the Zhurong landing site on Mars. *Natl Sci. Rev.* **10**, nwad056 (2023).

15. Mutch, T. A. et al. The surface of Mars: the view from the Viking 2 Lander. *Science* **194**, 1277–1283 (1976).

16. Maurice, S. et al. In situ recording of Mars soundscape. *Nature* **605**, 653–658 (2022).

17. Du, A. et al. Ground magnetic survey on Mars from the Zhurong rover. *Nat. Astron.* **7**, 1037–1047 (2023).

18. Hamran, S. E. et al. Radar imager for Mars' subsurface experiment—RIMFAX. *Space Sci. Rev* **216**, 128 (2020).

19. Zhou, B. et al. The Mars rover subsurface penetrating radar onboard China's Mars 2020 mission. *Earth Planet. Phys.* **4**, 345–354 (2020).

20. Hamran, S. E. et al. Ground penetrating radar observations of subsurface structures in the floor of Jezero crater, Mars. *Sci. Adv.* **8**, eabp8564 (2022).

21. Li, C. et al. Layered subsurface in Utopia basin of Mars revealed by Zhurong rover radar. *Nature* **610**, 308–312 (2022).

22. Chen, R. et al. Martian soil as revealed by ground-penetrating radar at the Tianwen-1 landing site. *Geology* **51**, 315–319 (2023).

23. Picardi, G. et al. Performance and surface scattering models for the Mars Advanced Radar for Subsurface and Ionosphere Sounding (MARSIS). *Planet. Space Sci.* **52**, 149–156 (2004).

24. Seu, R. et al. SHARAD: The MRO 2005 shallow radar. *Planet. Space Sci.* **52**, 157–166 (2004).

25. Mellon, M. T. & Sizemore, H. G. The history of ground ice at Jezero crater Mars and other past, present, and future landing sites. *Icarus* **371**, 114667 (2022).

26. Liu, G., Chen, X., Du, J. & Wu, K. Random noise attenuation using *f–x* regularized nonstationary autoregression. *Geophysics* **77**, V61–V69 (2012).

27. Liu, Y. & Li, B. Streaming orthogonal prediction filter in the *t–x* domain for random noise attenuation. *Geophysics* **83**, F41–F48 (2018).

28. Zhao, J. et al. Geological characteristics and targets of high scientific interest in the Zhurong landing region on Mars. *Geophys. Res. Lett.* **48**, e2021GL094903 (2021).

29. Ivanov, M. A., Hiesinger, H., Erkeling, G. & Reiss, D. J. I. Mud volcanism and morphology of impact craters in Utopia Planitia on Mars: evidence for the ancient ocean. *Icarus* **228**, 121–140 (2014).

30. Parker, A. P. Stability of arrays of multiple edge cracks. *Eng. Fract. Mech.* **62**, 577–591 (1999).

31. Seibert, N. M. & Kargel, J. S. Small-scale Martian polygonal terrain: implications for liquid surface water. *Geophys. Res. Lett.* **28**, 899–902 (2001).

32. Brooker, L. M. et al. Clastic polygonal networks around Lyot crater, Mars: possible formation mechanisms from morphometric analysis. *Icarus* **302**, 386–406 (2018).

33. Levy, J., Head, J. & Marchant, D. Thermal contraction crack polygons on Mars: classification, distribution, and climate implications from HiRISE observations. *J. Geophys. Res. Planets* **114**, E01007 (2009).

34. McGill, G. E. & Hills, L. S. Origin of giant Martian polygons. *J. Geophys. Res. Planets* **97**, 2633–2647 (1992).

35. Mutch, T. A., Arvidson, R. E., Binder, A. B., Guinness, E. A. & Morris, E. C. The geology of the Viking Lander 2 site. *J. Geophys. Res.* **82**, 4452–4467 (1977).

36. Lucchitta, B. K. Mars and Earth: comparison of cold-climate features. *Icarus* **45**, 264–303 (1981).

37. McGill, G. E. Age and origin of large Martian polygons. *Lunar Planet. Sci. Conf.* **16**, 534–535 (1985).

38. Singleton, A. C., Osinski, G. R., Samson, C., Williamson, M. C. & Holladay, S. Electromagnetic characterization of polar ice-wedge polygons: implications for periglacial studies on Mars and Earth. *Planet. Space Sci.* **58**, 472–481 (2010).

39. Mellon, M. T. Small-scale polygonal features on Mars: seasonal thermal contraction cracks in permafrost. *J. Geophys. Res. Planets* **102**, 25617–25628 (1997).

40. Perrin, C. et al. Geometry and segmentation of Cerberus Fossae, Mars: implications for marsquake properties. *J. Geophys. Res. Planets* **127**, e2021JE007118 (2022).

41. Li, J. H. & Zhang, L. M. Study of desiccation crack initiation and development at ground surface. *Eng. Geol.* **123**, 347–358 (2011).

42. Tang, C. S., Cui, Y. J., Tang, A. M. & Shi, B. Experiment evidence on the temperature dependence of desiccation cracking behavior of clayey soils. *Eng. Geol.* **114**, 261–266 (2010).

43. Simon, M. N., Carter, L. M., Campbell, B. A., Phillips, R. J. & Mattei, S. Studies of lava flows in the Tharsis region of Mars using SHARAD. *J. Geophys. Res. Planets* **119**, 2291–2299 (2014).

44. Sager, C., Airo, A., Arens, F. L. & Schulze-Makuch, D. New type of sand wedge polygons in the salt cemented soils of the hyper-arid Atacama Desert. *Geomorphology* **373**, 107481 (2021).

45. Wolfe, S. A. et al. Contemporary sand wedge development in seasonally frozen ground and paleoenvironmental implications. *Permafr. Periglac. Process* **308**, 215–229 (2018).

46. Douglas, T. A. & Mellon, M. T. Sublimation of terrestrial permafrost and the implications for ice-loss processes on Mars. *Nat. Commun.* **10**, 1716 (2019).

47. Morison, A., Labrosse, S. & Choblet, G. Sublimation-driven convection in Sputnik Planitia on Pluto. *Nature* **600**, 419–423 (2021).

48. Marchant, D. R. & Head, J. W. III Antarctic dry valleys: microclimate zonation, variable geomorphic processes, and implications for assessing climate change on Mars. *Icarus* **192**, 187–222 (2007).

49. Ye, B. et al. Geomorphologic exploration targets at the Zhurong landing site in the southern Utopia Planitia of Mars. *Earth Planet. Sci. Lett.* **576**, 117199 (2021).

50. Wordsworth, R. et al. A coupled model of episodic warming, oxidation and geochemical transitions on early Mars. *Nat. Geosci.* **14**, 127–132 (2021).

51. Laskar, J. et al. Long term evolution and chaotic diffusion of the insolation quantities of Mars. *Icarus* **170**, 343–364 (2004).

52. Clifford, S. M. & Parker, T. J. The evolution of the Martian hydrosphere: implications for the fate of a primordial ocean and the current state of the northern plains. *Icarus* **154**, 40–79 (2001).

53. Liu, Y. et al. Zhurong reveals recent aqueous activities in Utopia Planitia, Mars. *Sci. Adv.* **8**, eabn8555 (2022).

54. Liu, C. et al. Aqueous alteration of the Vastitas Borealis Formation at the Tianwen-1 landing site. *Commun. Earth Environ.* **3**, 280 (2022).

55. Qin, X. et al. Modern water at low latitudes on Mars: potential evidence from dune surfaces. *Sci. Adv.* **9**, eadd8868 (2023).

56. Lucchitta, B. K., Ferguson, H. & Summers, C. Sedimentary deposits in the northern lowland plains, Mars. *J. Geophys. Res. Solid Earth* **91**, E166–E174 (1986).

57. Zhang, J. et al. Volcanic history of the Imbrium basin: a close-up view from the lunar rover Yutu. *Proc. Natl Acad. Sci. USA* **112**, 5342–5347 (2015).

58. Zhang, J. et al. Lunar regolith and substructure at Chang'E-4 landing site in South Pole–Aitken basin. *Nat. Astron.* **5**, 25–30 (2021).

59. Liu, Y. & Fomel, S. Seismic data analysis using local time–frequency decomposition. *Geophys. Prospect.* **61**, 516–525 (2013).

60. Saha, J. Relationship between Fourier and instantaneous frequency. *SEG Tech. Program Expand. Abstr.* **1987**, 591–594 (1987).

61. Lovell, B. C., Williamson, R. C. & Boashash, B. The relationship between instantaneous frequency and time–frequency representations. *IEEE Trans. Signal Process.* **41**, 1458–1461 (1993).

62. Liu, G., Fomel, S. & Chen, X. Time–frequency analysis of seismic data using local attributes. *Geophysics* **76**, P23–P34 (2011).

63. Liu, J. et al. Geomorphic contexts and science focus of the Zhurong landing site on Mars. *Nat. Astron.* **6**, 65–71 (2022).

64. Ding, L. et al. Surface characteristics of the Zhurong Mars rover traverse at Utopia Planitia. *Nat. Geosci.* **15**, 171–176 (2022).

65. Liang, X. et al. The navigation and terrain cameras on the Tianwen-1 Mars rover. *Space Sci. Rev.* **217**, 37 (2021).

66. Liu, C., Tang, C., Shi, B. & Suo, W. Automatic quantification of crack patterns by image processing. *Comput. Geosci.* **57**, 77–80 (2013).

67. Zhang, L., Lu, Y. & Zhang, J. A polygonal terrain on Martian southern polar cap: implication for its formation mechanism. *Remote Sens.* **14**, 5789 (2022).

68. Sezer, G. İ., Ramyar, K., Karasu, B., Göktepe, A. B. & Sezer, A. Image analysis of sulfate attack on hardened cement paste. *Mater. Des.* **29**, 224–231 (2008).

69. Chambolle, A., Caselles, V., Novaga, M., Cremers, D. & Pock, T. An introduction to total variation for image analysis. *Theor. Found. Numer. Methods Sparse Recovery* **9**, 227 (2010).

70. Barrett, A. M. *An Investigation of Potential Periglacial Landforms on the Northern Plains of Mars: An Integrated Field, Laboratory and Remote Sensing Study*. PhD thesis, Open Univ. (2014).

71. Yoshikawa, K. Origin of the polygons and the thickness of Vastitas Borealis Formation in Western Utopia Planitia on Mars. *Geophys. Res. Lett.* **30**, 1603 (2003).

72. Ulrich, M., Hauber, E., Herzschuh, U., Härtel, S. & Schirrmeister, L. Polygon pattern geomorphometry on Svalbard (Norway) and western Utopia Planitia (Mars) using high-resolution stereo remote-sensing data. *Geomorphology* **134**, 197–216 (2011).

Acknowledgements

Author contributions

J.Z. conceptualized the project. C.L., L.Z., J.Z., B.Z., Yike Liu, X.Z., J.H., Y.Z., Y. Wang, X.W., W. Lv, Yang Li, H. Lan, Yuxi Li, W.W., G.F. and Z.Y. were responsible for the methodology. L.Z., C.L., J.Z., Y.S.Z., Yang Liu, K.D., R.N.M., J.L., Z.Z., Lin Chen, X.L., W.S., C.X., P.Z., Yang Li, H. Lin, P.F., W. Lin, Y. Wei, Ling Chen, Y. Lu and Y.P. interpreted the results. L.Z., C.L. and J.Z. carried out the investigation. L.Z., C.L. and J.Z. were responsible for visualization. J.Z. and Y.P. supervised the project. L.Z., C.L. and J.Z. wrote the original draft. All authors were involved in writing, reviewing and editing the final paper.

Competing interests

The authors declare no competing interests.

Additional information

Extended data are available for this paper at https://doi.org/10.1038/s41550-023-02117-3.

Supplementary information The online version contains supplementary material available at https://doi.org/10.1038/s41550-023-02117-3.

Correspondence and requests for materials should be addressed to Jinhai Zhang.

Peer review information *Nature Astronomy* thanks Shannon Hibbard and the other, anonymous, reviewer(s) for their contribution to the peer review of this work.

Reprints and permissions information is available at www.nature.com/reprints.

Publisher's note Springer Nature remains neutral with regard to jurisdictional claims in published maps and institutional affiliations.

¹CAS Engineering Laboratory for Deep Resources Equipment and Technology, Institute of Geology and Geophysics, Chinese Academy of Sciences, Beijing, China. ²Key Laboratory of Earth and Planetary Physics, Institute of Geology and Geophysics, Chinese Academy of Sciences, Beijing, China. ³Key Laboratory of Electromagnetic Radiation and Detection Technology, Aerospace Information Research Institute, Chinese Academy of Sciences, Beijing, China. ⁴GBA Branch of Aerospace Information Research Institute, Chinese Academy of Sciences, Guangzhou, China. ⁵International Center for Planetary Science, College of Earth Science, Chengdu University of Technology, Chengdu, China. ⁶Center for Lunar and Planetary Sciences, Institute of Geochemistry, Chinese Academy of Sciences, Guiyang, China. ⁷Center for Excellence in Comparative Planetology, Chinese Academy of Sciences, Hefei, China. ⁸State Key Laboratory of Space Weather, National Space Science Center, Chinese Academy of Sciences, Beijing, China. ⁹State Key Laboratory of Remote Sensing Science, Aerospace Information Research Institute, Chinese Academy of Sciences, Beijing, China. ¹⁰State Key Laboratory of Lithospheric Evolution, Institute of Geology and Geophysics, Chinese Academy of Sciences, Beijing, China. ¹¹College of Earth and Planetary Sciences, University of Chinese Academy of Sciences, Beijing, China. ¹²Key Laboratory of Petroleum Resource Research, Institute of Geology and Geophysics, Chinese Academy of Sciences, Beijing, China. ¹³College of Water Conservancy and Hydropower Engineering, Hohai University, Nanjing, China. ¹⁴These authors contributed equally: Lei Zhang, Chao Li. ✉e-mail: zjh@mail.iggcas.ac.cn
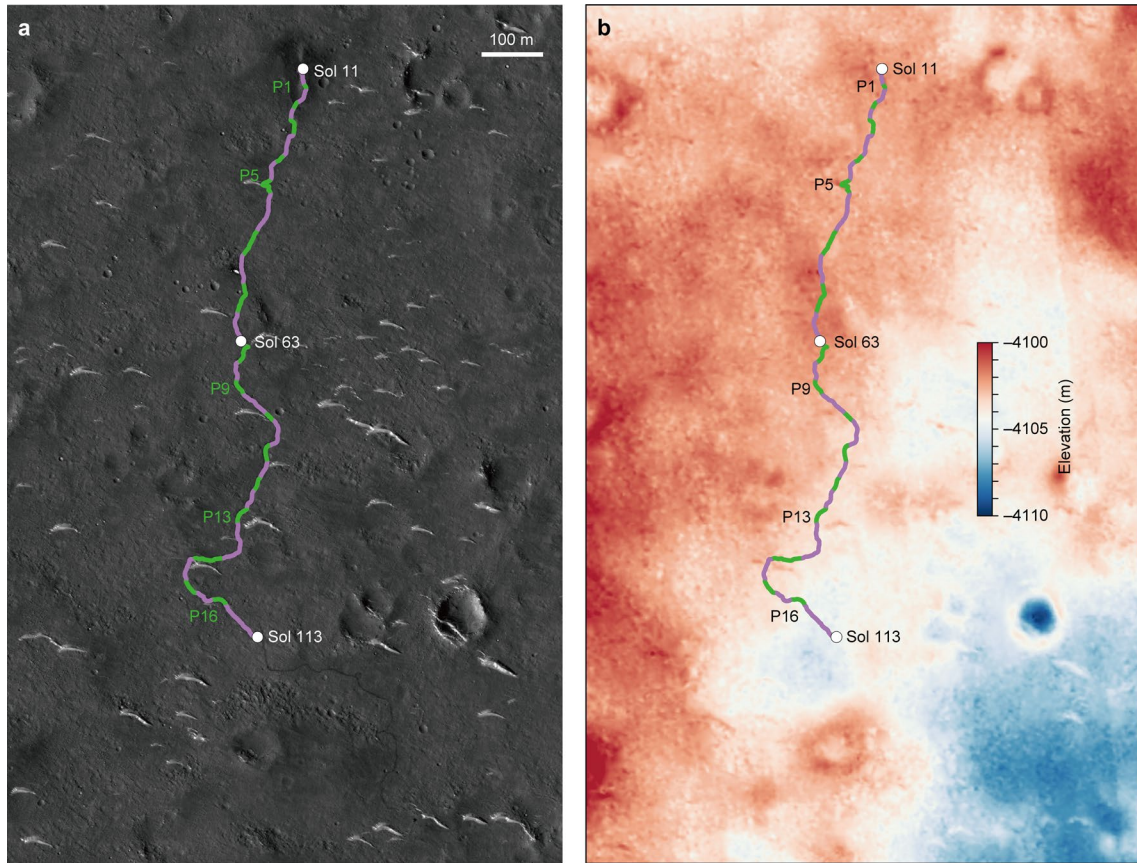
Extended Data Fig. 1 | Topography around the Zhurong landing site. a, HiRISE image with traverse of the Zhurong rover (similar to Fig. 1b). **b**, Elevation distribution around Zhurong landing site, obtained from ESP_073225_2055. Image credit of HiRISE: NASA/JPL/University of Arizona.
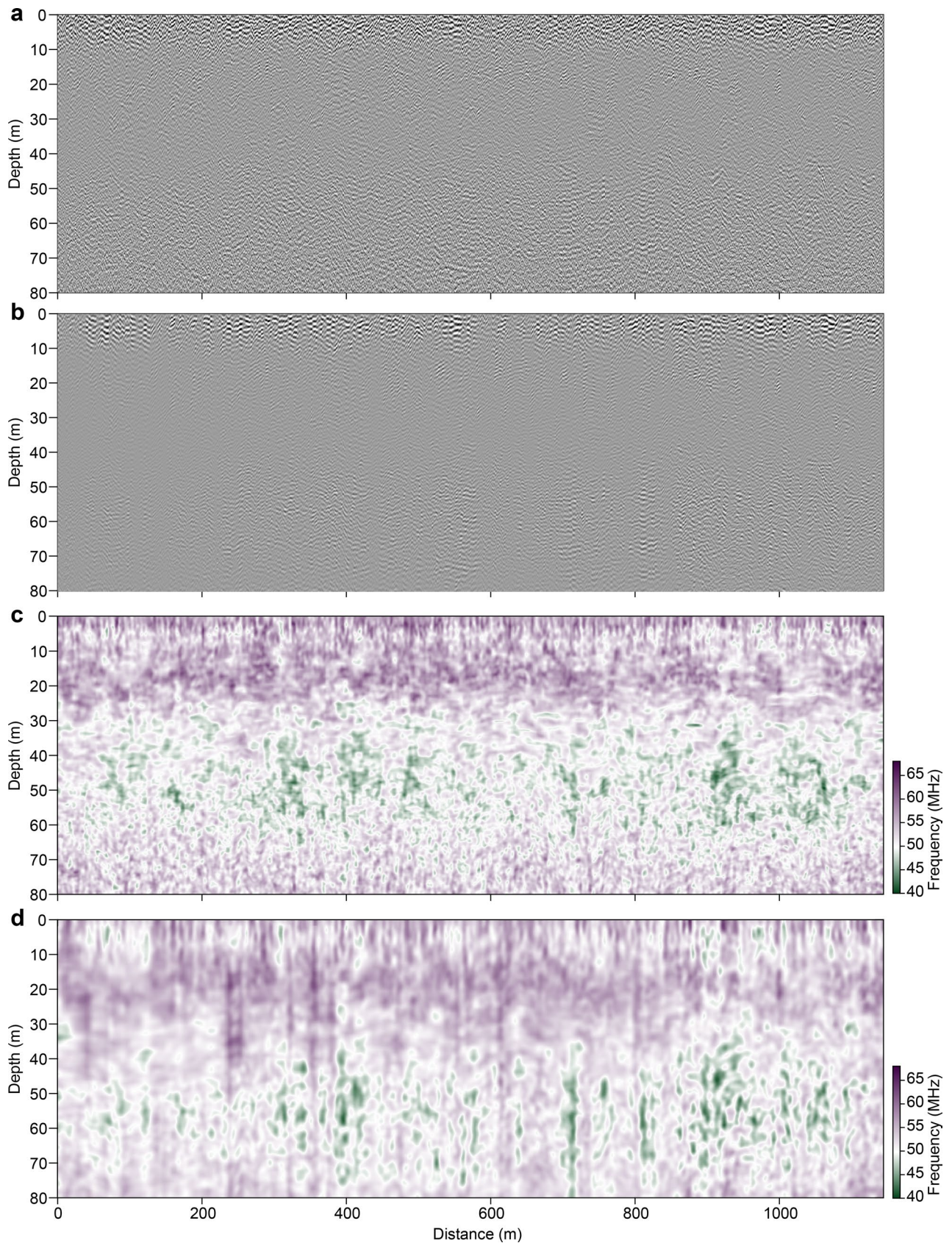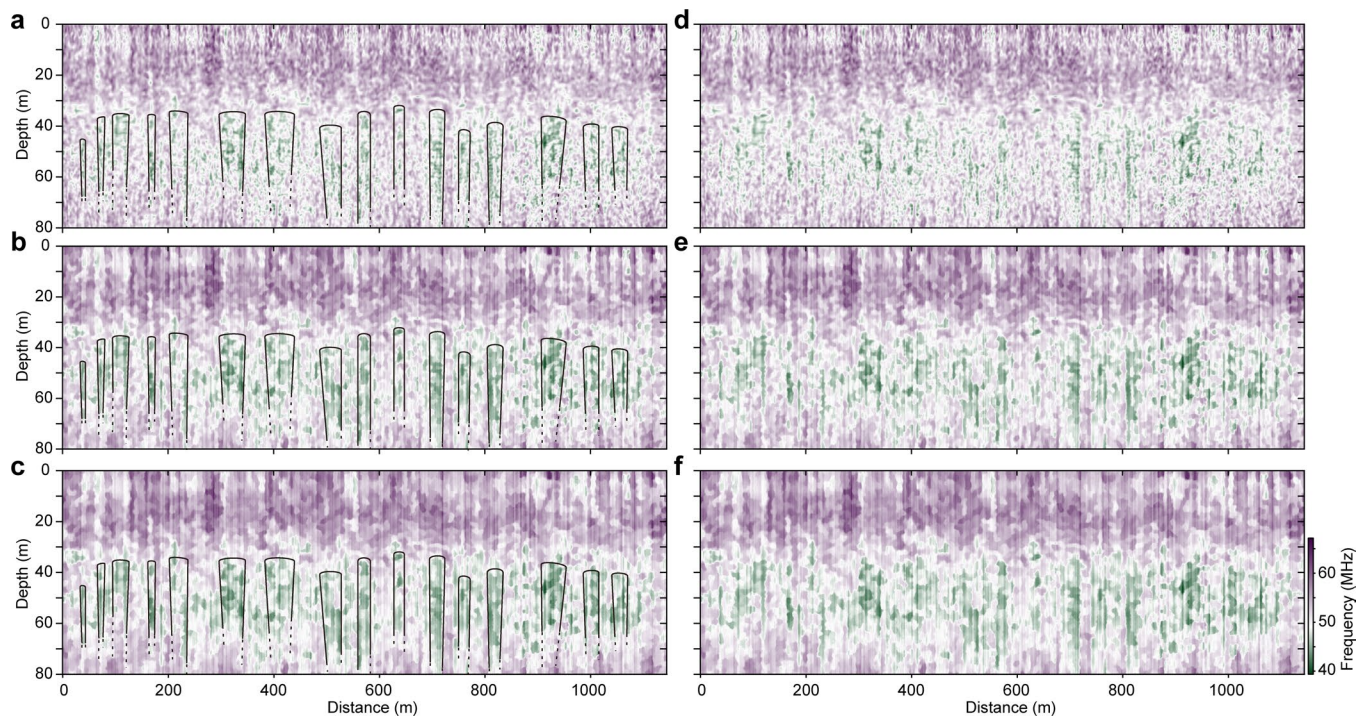
Extended Data Fig. 2 | Low-frequency profile of GPR and its corresponding time-varying average frequency. a, Before random noise attenuation. **b**, After random noise attenuation using the streaming orthogonal prediction filter method. **c**, The corresponding time-varying average frequency of **a. d**, The corresponding time-varying average frequency of **b**.
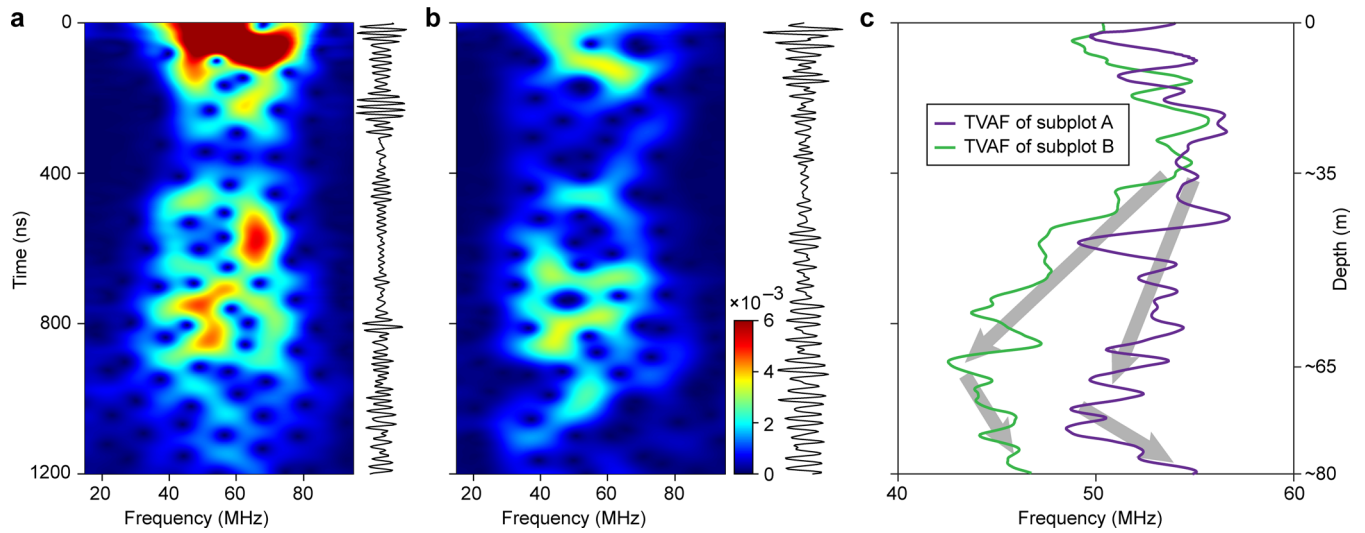
Extended Data Fig. 3 | Time-frequency map and time-varying average frequency of a single trace. a, Time-frequency map (left), and waveform (right) of trace at the distance of 666.5 m (in the polygon interiors, indicated by purple color in Fig. 2c). **b**, Time-frequency map (left), and waveform (right) of trace at the distance of 712.5 m (at the wedge of polygons, indicated by green color in Fig. 2c). **c**, Time-varying average frequency of **a** and **b**, where the grey arrows indicate the trend of different time-varying average frequencies.

Extended Data Fig. 4 | GPR imaging results using total variation (TV) regularization. a, Original time-varying average frequency profile, the same as Fig. 2a. **b**, The time-varying average frequency profile after applying TV regularization with a Lagrange multiplier $\lambda = 0.25$ (ref. 69). **c**, The time-varying average frequency profile after applying TV regularization with $\lambda = 0.20$. A smaller value of λ implies more aggressive suppression of local variations and tends to produce much larger patches. **d-f**, The same as **a-c** but without presenting the outlines of the low-frequency bands (black lines) for comparison.
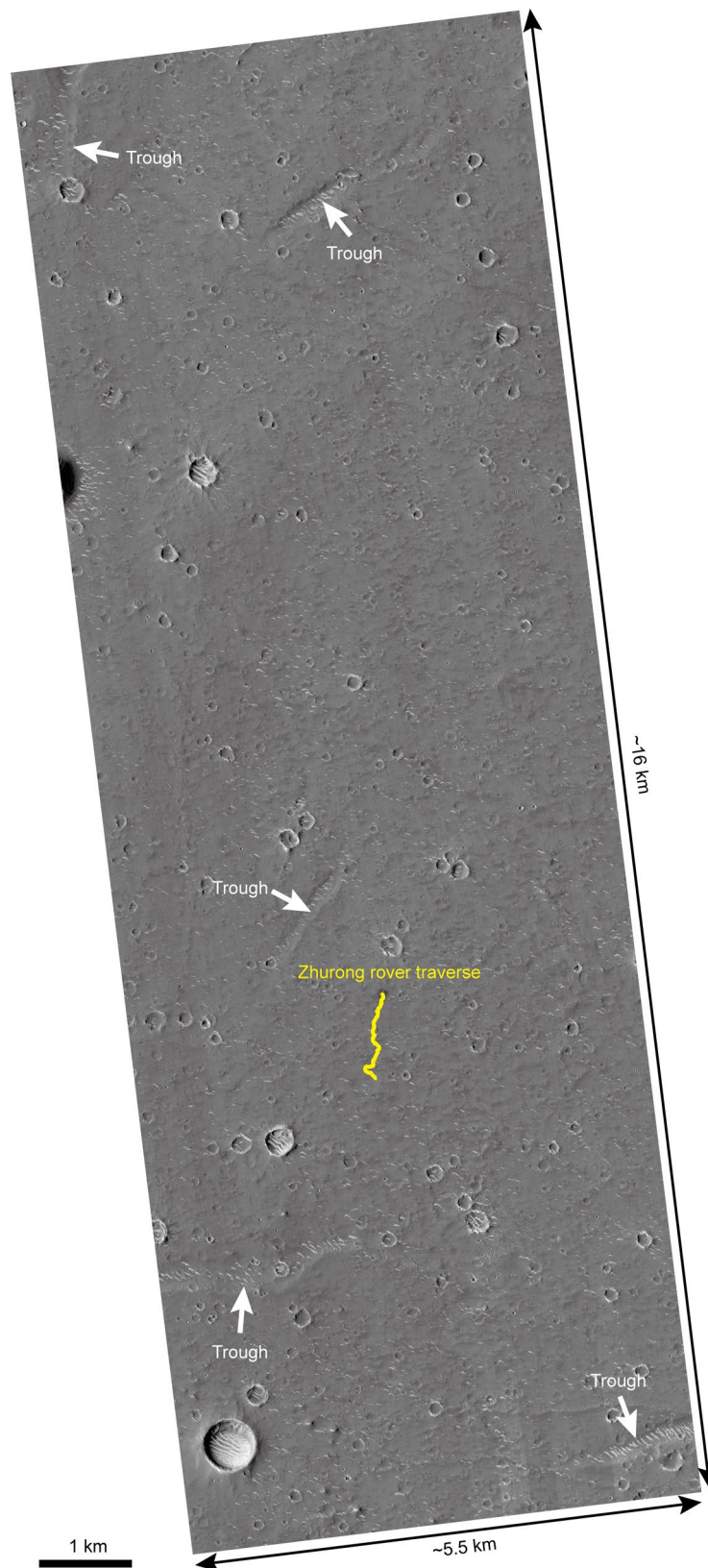
Extended Data Fig. 5 | Distribution of troughs around the Zhurong landing site. Trough locations are marked with white arrows. The Zhurong rover traverse (~1.2 km long) is marked as a yellow line. Image credit of HiRISE: NASA/JPL/University of Arizona.
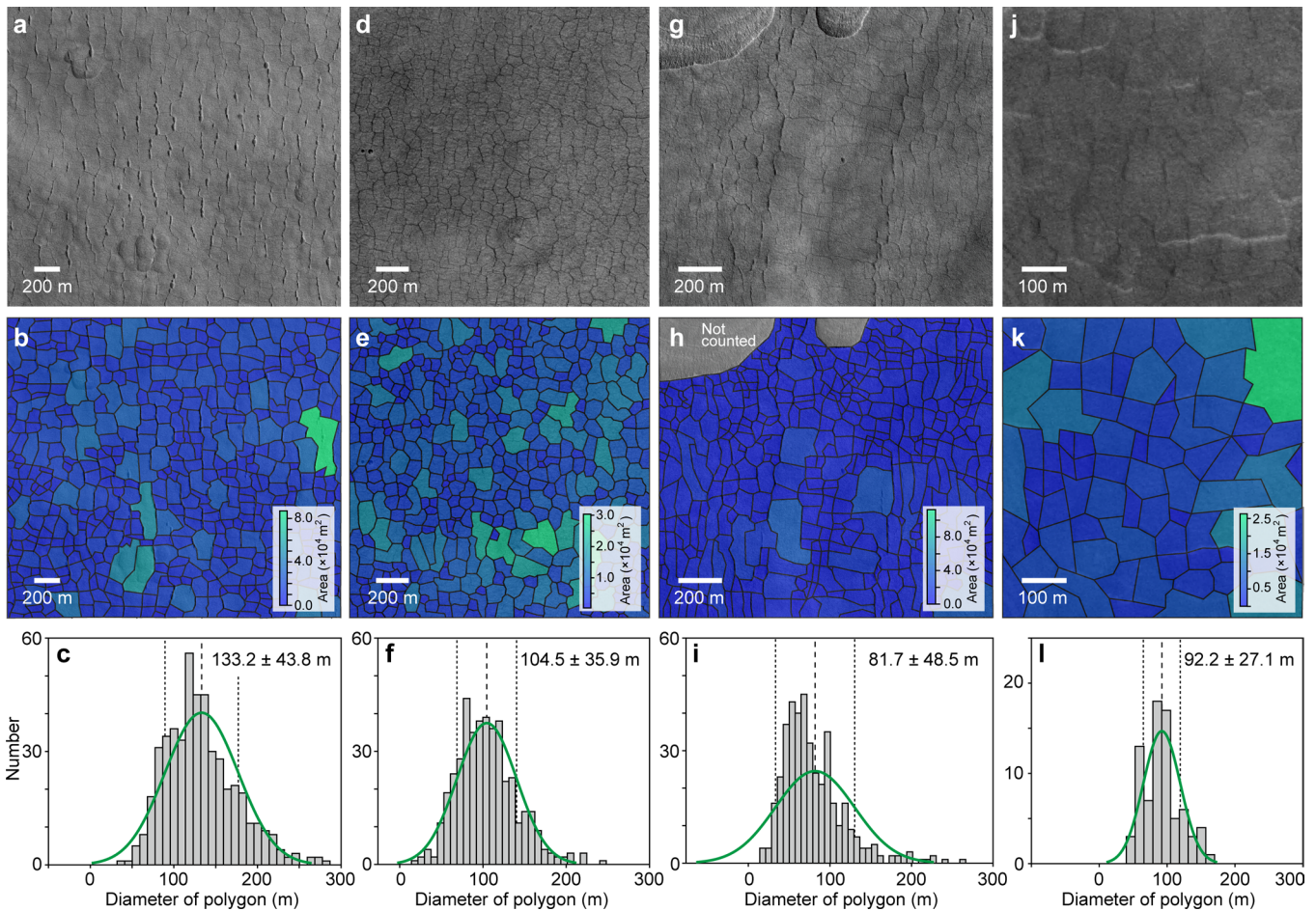
Extended Data Fig. 6 | Polygon diameter determination of four local regions with polygonal terrain. a, HiRISE images (Fig. 1c, PSP_002202_2250) in western Utopia Planitia, with locations marked in Fig. 1a. **b**, Recognized polygons based on manually mapped wedges of the polygons in **a. c**, Average diameter of the polygons shown in **b** using an imaging processing technology of the crack network[66,67]. The average diameter is defined as average of the maximum and the minimum Feret diameters. **d-f**, Same as **a-c** but for the HiRISE image PSP_006962_2215 (Fig. 1d). **g-i**, Same as **a-c** but for the HiRISE image PSP_002162_2260 (Fig. 1e). The two craters in the north are not counted for size analysis. **j-l**, Same as **a-c** but for the HiRISE image PSP_003177_2275 (Fig. 1f). Image credit: NASA/JPL/University of Arizona.

Planet	Location	Latitude (°)	Longitude (°)	Diameter (m)	SD (m)
Earth	Skagi, Iceland	66.0 N	23.8 W	0.3	—
	Tindastoll, Iceland	65.8 N	19.8 W	4.0	0.9
	Dry Valley, Antarctic	77.7 S	162.4 E	12.7	—
	Barrow, Alaska	71.3 N	156.8 W	16.3	—
	Adventdalen, Svalbard	78.2 N	16.3 E	29.7	1.4
	Pingo dal, East Greenland	69.4 N	133.1 W	38.2	—
Mars	Lomonosov	59.9 N	29.7 E	21.4	5.9
	Lyot crater	50.8 N	330.7 W	130.5	56.2
	Utopia Planitia (Fig. 1f)	46.950 N	101.833 E	92.2	27.1
	Utopia Planitia (Fig. 1e)	45.613 N	93.684 E	81.7	48.5
	Utopia Planitia (Fig. 1c)	44.724 N	84.441 E	133.2	43.8
	Utopia Planitia (Fig. 1d)	41.322 N	90.095 E	104.5	35.9
	Zhurong landing site	25.1 N	109.9 E	67.4	23.5
	South Polar Layered Deposit	87.0 S	—	137.7	—

Extended Data Fig. 7 | Polygon diameter in polygonal geomorphology on Earth and Mars[32,70,71,72].
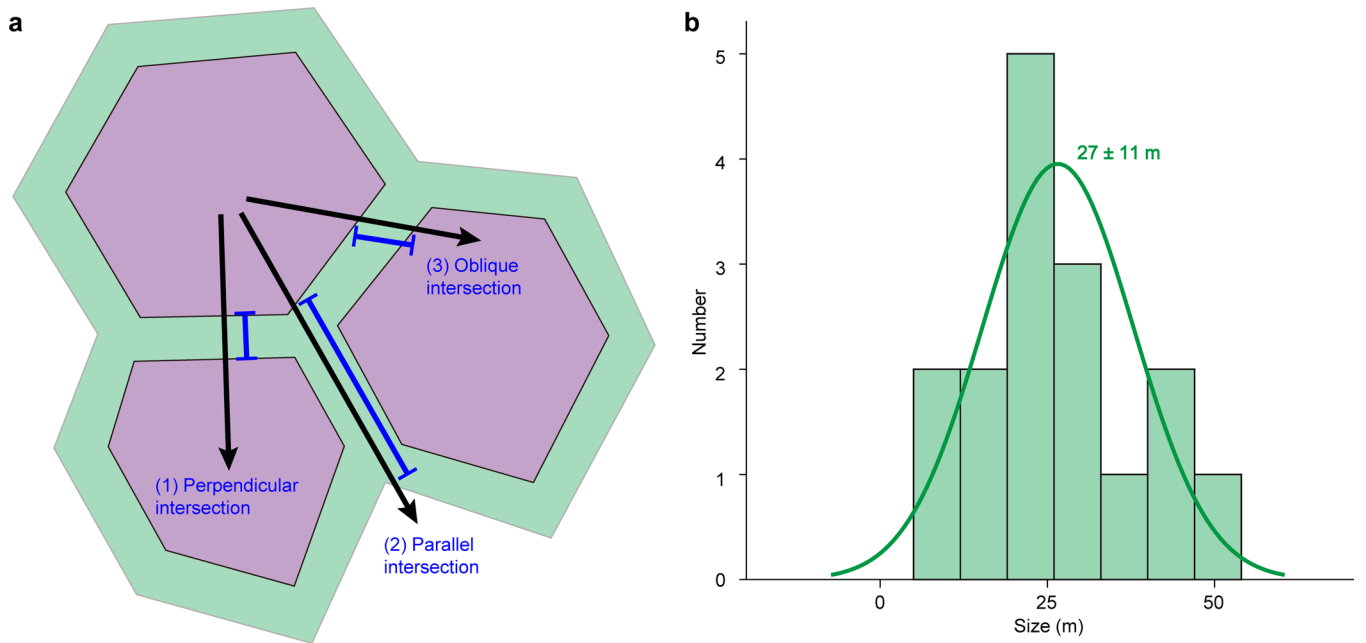
Extended Data Fig. 8 | Illustration of the apparent width of low-frequency band recognized in Fig. 2a. a, Sketch map of the relative location of the rover track and polygon wedges. **b**, Histogram of wedge width recognized from Fig. 2b.
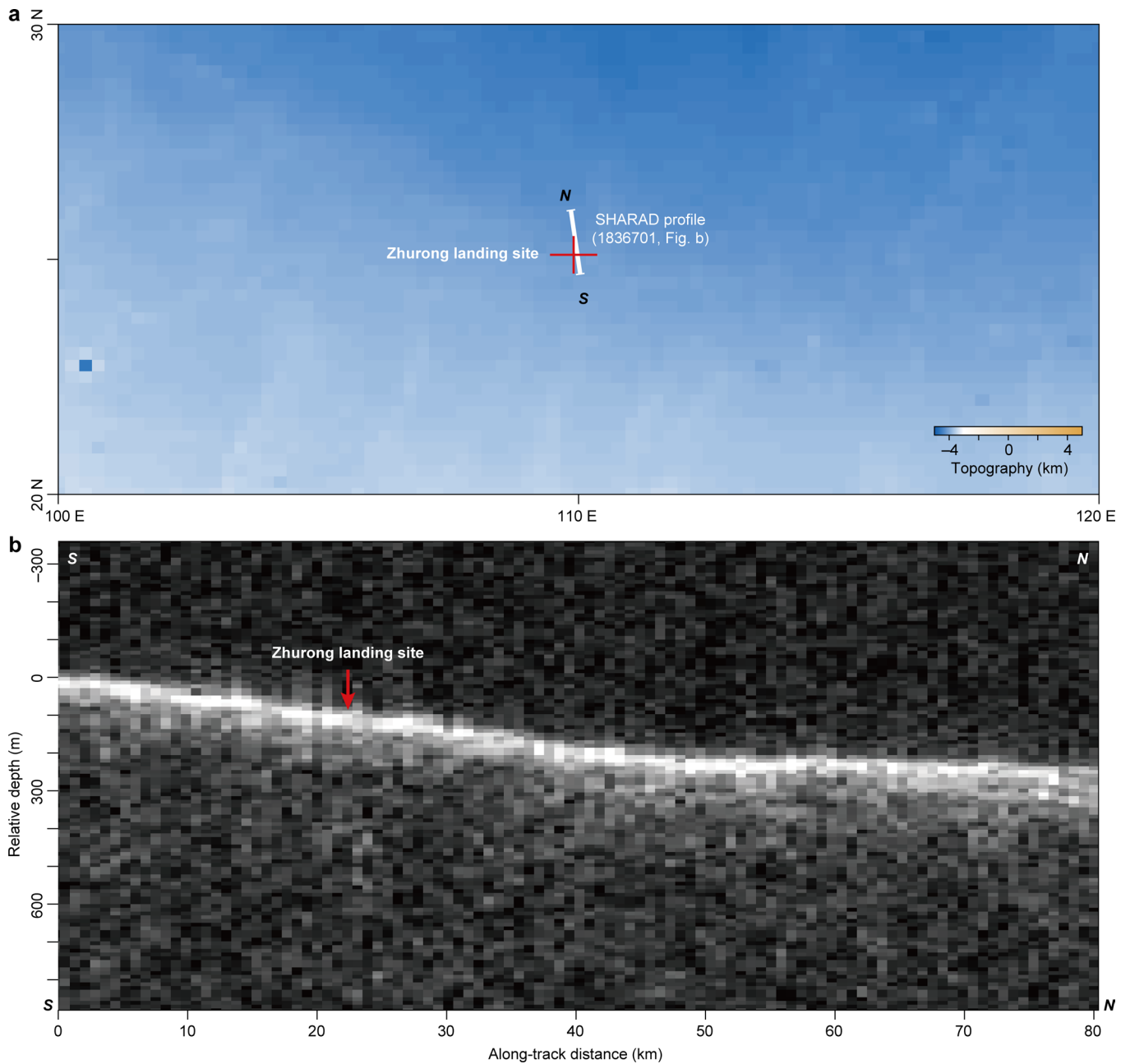
Extended Data Fig. 9 | Topographic map around the Zhurong landing site and the related SHARAD profile. a, The elevation distribution around the Zhurong landing site (red cross). An N-S profile of SHARAD data is marked as a white line. **b**, SHARAD radargram (s_01836701) near the Zhurong landing site. Note that the vertical axis is the depth relative to Point S. The Zhurong landing site is marked as a red arrow.